

Multi-Purpose Fully Differential 61- and 122-GHz Radar Transceivers for Scalable MIMO Sensor Platforms

Herman Jalli Ng, *Member, IEEE*, Maciej Kucharski, *Member, IEEE*, Wael Ahmad, and Dietmar Kissinger, *Senior Member, IEEE*

Abstract—This paper describes a multi-purpose radar system suitable for applications with different requirements on dynamic range, resolution, and miniaturization degree. It utilizes a scalable sensor platform that includes a wideband 30.5-GHz voltage-controlled oscillator (VCO) as well as 61- and 122-GHz transceivers (TRXs) in a silicon–germanium BiCMOS technology. The proposed architecture enables the cascading of multiple TRXs and allows the implementation of MIMO radar systems in two different frequency bands by using a single VCO. The higher transmit output power of 11.5 dBm as well as receive gain of 24 dB make the 61-GHz TRX suitable for applications requiring a high dynamic range. The lower wavelength allows the integration of on-chip antennas in the 122-GHz TRX and enables, thus, a high miniaturization degree. The higher LO scaling factor makes the 122-GHz TRX also more attractive for high-resolution applications. A sweep bandwidth of 2.5 GHz generated by the VCO is scaled up to 10 GHz and results in a range resolution of 3 cm. The proposed TRXs are equipped with binary phase shift keying modulators as well as an I/Q receiver and can be utilized to build a flexible software-defined radar platform for range and distant-selective vibration sensors utilizing frequency-modulated continuous wave as well as pseudo-random noise radar techniques.

Index Terms—122-GHz radar, 61-GHz radar, Doppler, double folded dipole antenna, frequency-modulated continuous wave (FMCW), millimeter wave integrated circuits, MIMO radar, on-chip antenna, pseudo-random noise (PRN), scalable radar transceiver (TRX), silicon–germanium technology, system-on-chip (SoC).

I. INTRODUCTION

RECENT advances achieved in silicon–germanium (SiGe) BiCMOS technologies in terms of high-frequency characteristics paved the way for the implementation of integrated circuits in the mm-wave frequency region, which offers an unprecedented level of resolution and an extremely high miniaturization potential [1], [2]. These technologies enable a high integration level with moderate mask costs and show

Manuscript received December 20, 2016; revised April 5, 2017; accepted May 4, 2017. Date of publication June 6, 2017; date of current version August 22, 2017. This paper was approved by Guest Editor Sorin P. Voinigescu. This work was supported by the German Bundesministerium für Bildung und Forschung through the Research Project radar4FAD. (*Corresponding author: Herman Jalli Ng.*)

H. J. Ng, M. Kucharski, and W. Ahmad are with IHP GmbH, 15236 Frankfurt (Oder), Germany (e-mail: herman.j.ng@ieee.org; kucharski@ihp-microelectronics.com; ahmad@ihp-microelectronics.com.)

D. Kissinger is with the Institute of High-Frequency and Semiconductor System Technologies, Technische Universität Berlin, 10587 Berlin, Germany, and also with IHP GmbH, 15236 Frankfurt (Oder), Germany (e-mail: kissinger@ieee.org).

Color versions of one or more of the figures in this paper are available online at <http://ieeexplore.ieee.org>.

Digital Object Identifier 10.1109/JSSC.2017.2704602

the most promise for the analog and mixed-signal-integrated circuits in next generation commercial applications [3].

Depending on the application areas, radar sensors often have different requirements of dynamic range, resolution, and miniaturization degree. High dynamic range is required for the detection of targets with very low reflectivity such as non-metallic parts. Targets with a small radar cross section (RCS) result in a low receive signal. These targets can be detected with an acceptable signal-to-noise ratio (SNR) by using a radar system with a high dynamic range that is more easily provided at a lower operating frequency. High resolution is of particular importance for the distinction of targets that are very close together as well as for the detection of targets located close to the radar transceiver (TRX). A high-resolution radar requires a high modulation bandwidth that is more easily provided by a radar system operating at a higher center frequency. Highly miniaturized sensors are particularly desirable for sensing applications where the total weight and size are tightly specified, for example in small unmanned aerial vehicles. The shrinking of the passive structures, such as antennas at a higher frequency, enables a high degree of miniaturization.

To provide the optimal dynamic range, resolution, and miniaturization degree, a scalable radar sensor architecture that combines a 30.5-GHz voltage-controlled oscillator (VCO) and radar TRXs operating at two different frequency bands is proposed [4]. The VCO has a maximum tuning range of 2.75 GHz and can provide an LO signal to the radar TRXs, which can be cascaded for MIMO applications. The 61-GHz TRX can deliver a higher TX output power, a higher RX gain, and a lower noise figure, since this operating frequency is much lower than the f_T/f_{max} of the SiGe technology. The 122-GHz TRX can achieve a higher modulation bandwidth due to the higher frequency scaling factor of the LO frequency. The higher operating frequency also enables the integration of the antennas directly on the chip and allows thus the miniaturization of the radar sensor [5]. The proposed TRXs are equipped with binary phase shift keying (BPSK) modulators as well as an in-phase/quadrature (I/Q) receiver and can be utilized as a base to build a very flexible software-defined radar platform.

II. SYSTEM ARCHITECTURE

Fig. 1 shows the overall system overview of the proposed scalable sensor platform consisting of a 30.5-GHz VCO and several multi-purpose 61- and 122-GHz TRXs. These TRXs

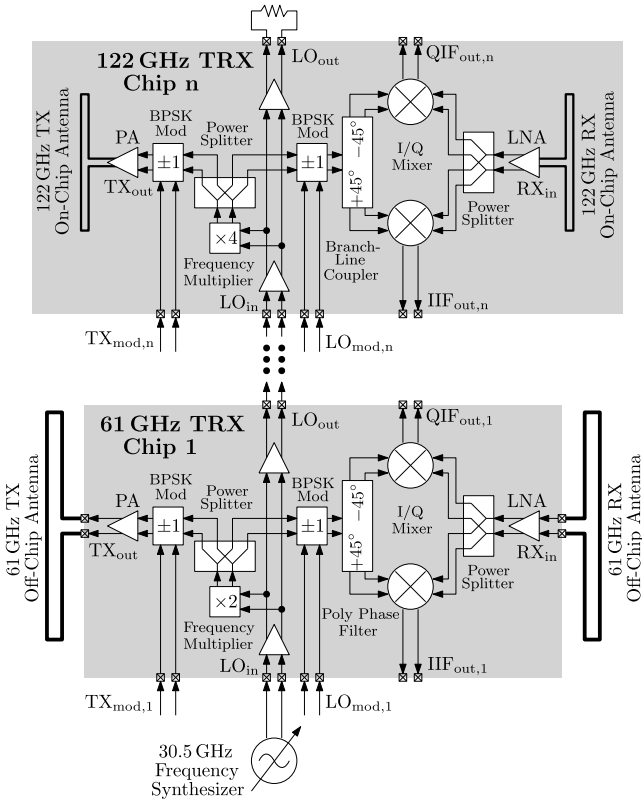


Fig. 1. Simplified block diagram of the proposed scalable sensor platform consisting of a 30.5-GHz frequency synthesizer and several multi-purpose 61- and 122-GHz TRXs that are cascaded to form a daisy chain.

require only a single 30.5-GHz LO signal from a separate VCO, which is complemented by a buffer as well as a prescaler and is stabilized by an external fractional-N PLL. Each TRX is equipped with an LO buffer to output the LO signal for the next TRX so that multiple TRXs can be cascaded to build a daisy chain. Compared with the solution reported in [6], the routing of the LO signal in the proposed architecture is much simpler and does not require any additional lossy LO distribution network such as planar Wilkinson dividers. A frequency multiplier inside each TRX scales up the LO frequency to 61 or 122 GHz. A power splitter provides the carrier signal to the TX path and the RX path. A power amplifier (PA) is used to drive the TX antenna. The I/Q receiver consists of a low-noise amplifier (LNA), two down-conversion mixers, and a 90° coupler, which is implemented as a poly-phase filter in the 61-GHz TRX and as a branch-line coupler in the 122-GHz TRX. Two BPSK modulators included in the TX and the RX path can be used to modulate the carrier signal with any binary sequences, for example a bit stream of a $\Delta\Sigma$ -modulator or a pseudo-random binary sequence (PRBS). In this way, the proposed flexible sensor platform can address several applications, such as conventional frequency-modulated continuous-wave (FMCW) MIMO radar with time division multiplexing (TDM) and frequency division multiplexing (FDM) [7], a pseudo-random noise (PRN) radar [8], [9], and a PRN-coded Doppler radar [10].

TABLE I
CURRENT CONSUMPTION OF BUILDING BLOCKS

Transceiver	61 GHz	122 GHz
3x 30.5-GHz LO buffer/pow.splitter	33 mA	33 mA
1x Freq.doubler 30.5 to 61 GHz	11 mA	11 mA
1x Freq.doubler 61 to 122 GHz	-	11 mA
4x 61/122-GHz buffer/pow.splitter	44 mA	44 mA
2x mixer	22 mA	22 mA
1x low noise amplifier	11 mA	11 mA
1x power amplifier	31 mA	31 mA
2x BPSK modulator	22 mA	22 mA
Total current consumption	174 mA	185 mA
Measured current consumption	180 mA	190 mA

III. TRANSCEIVERS

The proposed multi-purpose TRXs were developed from scratch to allow for a completely uniform and modular layout. Metal grids are utilized to create proper supply and ground planes throughout the chip. The fully differential circuit topology is strictly applied from the input up to the output stages, since the balanced design exhibits higher immunity to common-mode noise and provides an increased distortion-free dynamic range. Custom transmission lines (TLs) with defined characteristic impedances are used throughout the chip. The lumped component models for the single-ended and differential TLs were calculated using electromagnetic simulations. These TLs were used to create various arbitrary impedances, as equivalent inductors or capacitors, for the impedance matching and for the signal routing between the circuit blocks.

Fig. 2 shows the micrographs of the fabricated 61- and 122-GHz TRX chips, which were implemented in the IHP 130-nm SiGe BiCMOS technology with f_T/f_{\max} of 220/300 GHz and five thin as well as two thick metal layers [1]. Both chips have the same pad frame and size of $2.14 \text{ mm} \times 1.74 \text{ mm}$. The measured current consumption of the 61- and the 122-GHz TRX is 180 and 190 mA from 3.3-V supply, respectively. Table I shows the number and the current consumption of the building blocks used in the 61- and 122-GHz TRX at 3.3-V supply. Except for the PA, the core of each building block consumes 10 mA and the bias network consumes additional 1 mA of current. The 61- and the 122-GHz TRXs consist of building blocks using the same circuit topologies, bias networks, transistor sizes, and layout cores. The passive matching networks were adjusted to the respective center frequencies. The 122-GHz TRX includes an additional frequency doubler from 61 to 122 GHz that increases the current consumption by 11 mA.

Fig. 3 shows the measurement and simulation results of the TX output power and the RX voltage conversion gain of the 61- and the 122-GHz TRX. The differential measurement could only be performed on the 61-GHz TRX, while the 122-GHz TRX had to be characterized single-endedly due to the missing of suitable baluns at this frequency. A small discrepancy between the simulation and measurement result of the 122-GHz TRX can thus be observed. The 61-GHz transmitter achieves a maximum output power of 11.5 dBm

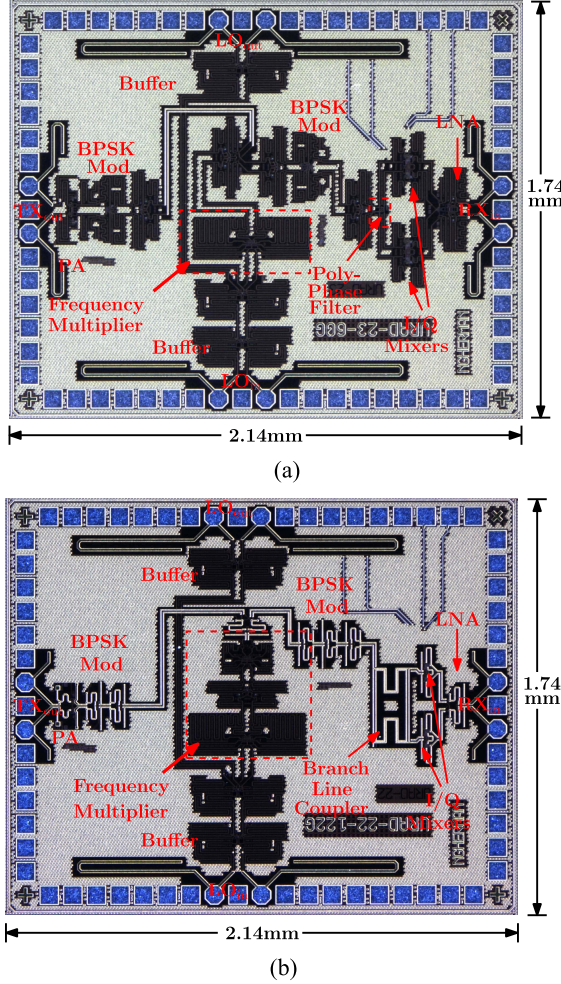


Fig. 2. Chip photograph of (a) 61- and (b) 122-GHz TRXs. Both chips have the same pad frame and size of $2.14 \times 1.74 \text{ mm}^2$.

at 61 GHz, while the measured maximum output power of the 122-GHz transmitter is 5 dBm at 120 GHz. The variation of the output power is small in a wide frequency range, enabling a broadband system operation. The 61-GHz receiver achieves a maximum RX conversion gain of 24 dB at 61 GHz, while the measured maximum RX conversion gain of the 122-GHz receiver is 21 dB at 122 GHz. The input referred 1-dB compression point ($P_{1\text{ dB}}$) is around -12 dBm for the 61-GHz receiver and -11 dBm for the 122-GHz receiver.

A. Amplifier and Gilbert-Cell Based Circuit Blocks

The proposed scalable sensor platform utilizes a number of amplifiers for different purposes and at three different frequency bands. The circuit topology is used to implement a buffer for the 30.5-GHz LO signal and an active power splitter to provide the TX and LO paths with a sufficient input power at 61 and 122 GHz. For these two purposes, the inputs and the outputs of the amplifiers are matched for optimum reflection coefficients. In a slightly modified version, the circuit topology is also used as a PA and as an LNA. The output of the PA is matched for a maximum output power, while the input of the LNA is matched for a minimum noise

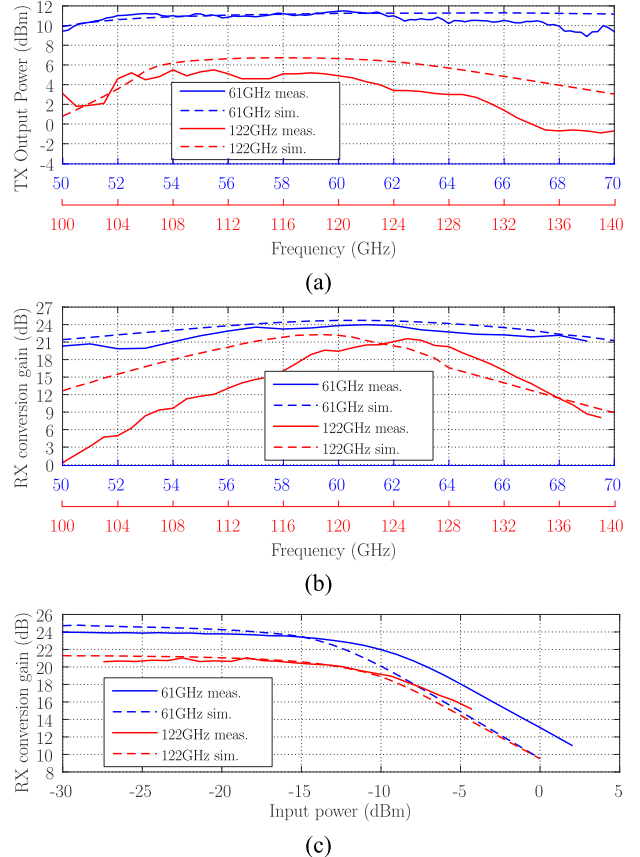


Fig. 3. Measurement and simulation results of the 61- and 122-GHz TRXs. (a) TX output power over the frequency. (b) RX voltage conversion gain over the frequency. (c) RX voltage conversion gain over the input power.

figure. In most cases, the amplifier is required to provide a significant gain and an isolation between its input and output. Fig. 4(a) shows the schematic of the amplifier implemented in a common-emitter configuration with a common-base cascode and inductor loads using microstrip TLs. The differential pair used as an input stage provides the transconductance, while the cascode increases the gain as well as enables a higher input-output isolation. A quasi-current mirror with a low headroom voltage is used to provide a tail current for the differential pair, which together with the tail resistor forms the mirrored current. Impedance matching is accomplished by using TLs and capacitors are employed as ac couplings at the input and the output of the circuit. The implemented amplifier consumes 10 mA from 3.3-V supply voltage and achieves a gain of 11–13 dB.

The amplifier circuit was used as a base to build other circuit blocks. Gilbert-cell circuits can be realized by adding two additional transistors to the common-base cascode to form a switching quad. Fig. 4(b) shows the implemented double-balanced mixer based on the Gilbert-cell circuit. The collectors of the switching quad are cross connected with the opposite phases to sum the output currents. Pull-up resistors are used as loads at the differential IF output. The implemented mixer achieves a voltage conversion gain of 11–13 dB.

The frequency multiplier is implemented as double-balanced Gilbert-cell-based frequency doublers from 30.5 to 61 GHz

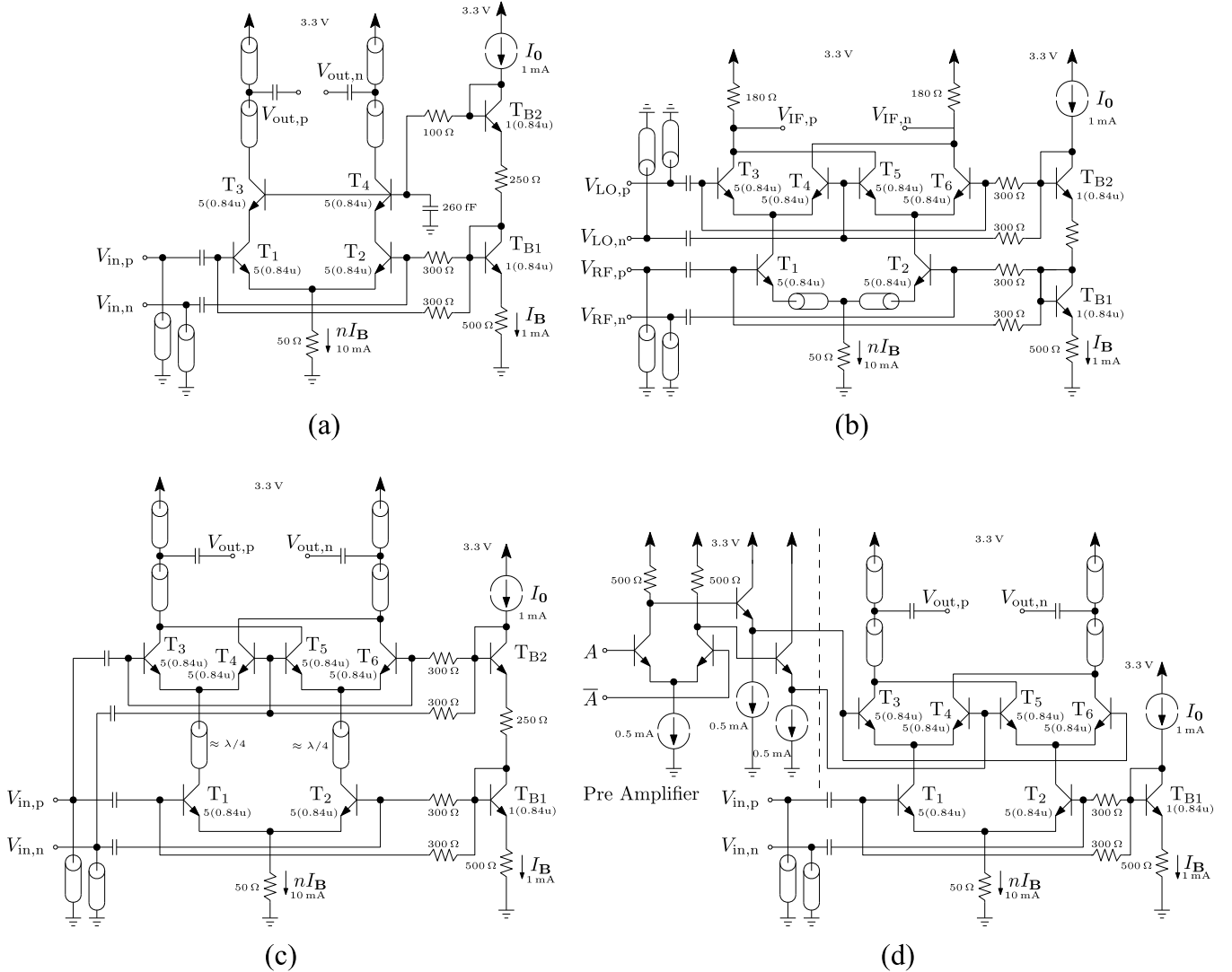


Fig. 4. Schematics of (a) 30.5-, 61-, and 122-GHz amplifiers implemented as a differential pair in a common-emitter configuration with a common-base cascode, (b) 61- and 122-GHz Gilbert-cell-based down-conversion mixer, (c) Gilbert-cell-based frequency doubler from 30.5 to 61 GHz and from 61 to 122 GHz, and (d) 61- and 122-GHz Gilbert-cell-based BPSK modulator.

and from 61 to 122 GHz. The schematic is shown in Fig. 4(c) and the measurement as well as simulation results were reported in [4]. Although both frequency doublers consume the same 10 mA from a 3.3-V supply voltage, the former exhibits a better performance compared with the latter, which works at a higher operating frequency closer to the f_T/f_{max} of the SiGe technology. The first frequency doubler achieves a conversion gain of 7.5 dB at -5-dBm input power and 61-GHz output frequency. The second frequency doubler achieves a conversion loss of 1.5 dB at -5-dBm input power and 122-GHz output frequency.

Fig. 4(d) shows the implemented BPSK modulator. Its core is also implemented in the Gilbert-cell topology that consists of a differential amplifier stage cascaded by a switching quad. The carrier signal is fed to this differential amplifier stage. Another differential pair followed by a pair of emitter-followers is used as a pre-amplifier for the conditioning of the differential digital input signal that is to be modulated on the carrier signal. Its differential output is fed to the switching quad of the BPSK modulator. A change of the polarity in the

digital signal results in a phase shift of 180° in the output signal of the BPSK modulator.

B. I/Q Receiver

The quadrature LO signals needed by the I/Q mixers to down-convert the RX signal are generated by using a poly-phase filter in the 61-GHz TRX and a branch-line coupler in the 122-GHz TRX. Fig. 5 shows the block diagrams. In both realizations, a one-stage amplifier is used to drive the poly-phase filter or the branch line coupler on the LO side and an LNA is used to drive the two down-conversion mixers on the RX side. The outputs of the two amplifiers provide an impedance matching to the input of the poly-phase filter or the branch line coupler and the two down-conversion mixers, respectively. In this way, the two mixers are always operated in the LO saturated region and the gain mismatch should be very small.

The branch line coupler can be efficiently implemented at higher frequency by using differential TLs due to the smaller wavelength. The coupler requires four segments of TLs, each

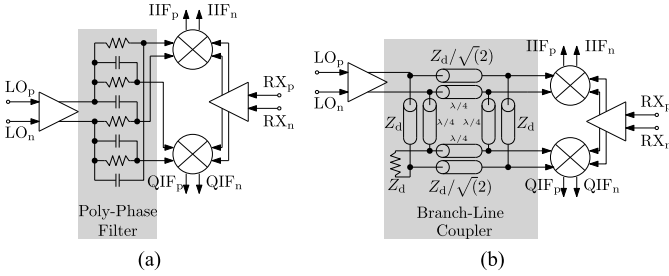


Fig. 5. Block diagram of (a) 61-GHz I/Q receiver with poly-phase filter and (b) 122-GHz I/Q receiver with branch-line coupler.

$\lambda/4$ in length, connected together to form a rectangular loop with four ports, and each port is formed by two segments of TLs with two different characteristic impedances, Z_d and $Z_d/\sqrt{2}$. The chosen characteristic port impedance Z_d of the differential TL used for this paper is $100\ \Omega$, and so the second characteristic impedance required for the branch line coupler is around $70\ \Omega$. The first port is used for the input signal, the second and third ports are for the in-phase and quadrature outputs, and the last port is terminated with a $100\text{-}\Omega$ resistor. The measured phase error of the I/Q receiver using the branch line coupler is around 5° at 122 GHz. At a lower frequency, the branch line coupler would require a huge chip area. The poly-phase filter using RC and CR networks also delivers a good accuracy at a lower frequency and requires a much smaller chip area [11]. The main idea is to use the RC and the CR networks to shift the phase of the input signal by -45° and $+45^\circ$, respectively, so that a phase difference of 90° between the in-phase and the quadrature output signal is achieved. The measured phase error of the I/Q receiver using the poly-phase filter is around 6° at 61 GHz.

C. Voltage-Controlled Oscillator

The 30.5-GHz VCO is implemented in the differential Colpitts topology that is characterized by its wide tuning range and superior phase noise (PN) performance due to the inherently isolated resonant circuit [12]–[14]. Its schematic is shown in Fig. 6(a). The Q -factor of the LC tank remains the bottleneck for the PN performance of the VCO. The frequency tuning element in the LC tank is the varactor, of which the Q -factor is lower compared with the tank inductor. A tradeoff between PN performance and tuning range has to be considered for different requirements. The implemented LC tank has a Q -factor of around 8, and the Q -factor of the inductor and the varactor is 28 and 11.5, respectively. Fig. 6(b) shows the simulated and measured characteristic line as well as the gain of the implemented VCO. The VCO has a maximum tuning range of 2.75 GHz and a maximum gain of larger than 2.5 GHz/V around the tuning voltage of 1.5 V. This measurement result reveals that the VCO in combination with a fractional-N PLL can be used to generate a frequency sweep of at least 2.5 GHz. The gain variation over the VCO tuning range is compensated by the feedback loop, resulting in a high FMCW linearity.

D. 122-GHz On-Chip Antenna

The higher frequency band of 122 GHz is advantageous for the implementation of miniaturized system-on-chip (SoC)

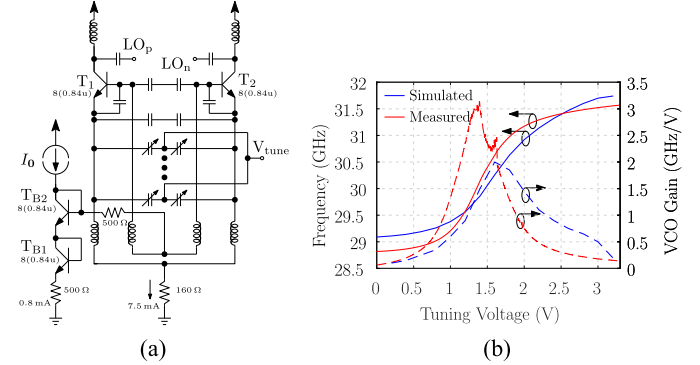


Fig. 6. (a) Schematic of the 30.5-GHz differential Colpitts VCO. (b) Measured and simulated characteristic line as well as gain of the implemented VCO.

radar sensor. The wavelength at this frequency band is small enough to allow the integration of the antenna directly on the chip. Fig. 7(a) shows the implemented 122-GHz SoC radar sensor with the on-chip antennas that are realized as double-folded dipole antenna using the localized backside etching (LBE) technique [15]. A selective etching technique introduced in [5] is utilized to selectively remove the silicon in critical areas under the antenna to improve the radiation efficiency and the mechanical stability of the chip. Using the LBE technique, the gain of the on-chip antenna can be improved by 2–4 dB, depending on the size of the etching area, the width of the side walls, and the thickness of the substrate. Fig. 8 shows the measurement and simulation results of the antenna gain and radiation patterns. An antenna gain of up to 6 dBi was measured, while the simulated radiation efficiency is about 54% at 122 GHz. A discrepancy between the simulation and measurement result at frequencies lower than 118 GHz and higher than 137 GHz might be caused mainly by the limitation of the probe-based F -band measurement setup and, to a smaller extent, by the inaccurate model of the permittivity/conductivity of the silicon oxide, especially at very high frequency. The measured 3-dB beamwidth in E -plane (xz plane) and H plane (yz plane) is 44° and 50° , respectively.

IV. SYSTEM APPLICATIONS

A. FMCW Radar and $\Delta\Sigma$ -Modulator-Based Frequency Division Multiplexing

The main idea of the FMCW radar is to modulate the frequency of the TX signal linearly in the time domain in order to gain the information of its round trip delay time (RTDT) τ_0 in the frequency domain [16]–[18]. Fig. 9 shows the basic principle of the FMCW chirp and the transformation of the RTDT τ_0 into the frequency difference of the TX and the RX signal.

The proposed scalable sensor architecture enables the cascading of multiple TRXs to build an MIMO radar system using TDM and FDM. In the FDM mode, the distinction of the TX signals is achieved by modulating the carrier signal with a different offset frequency for each TX channel. Several FDM-based systems that require additional effort to generate the frequency-shifted TX signals have been reported

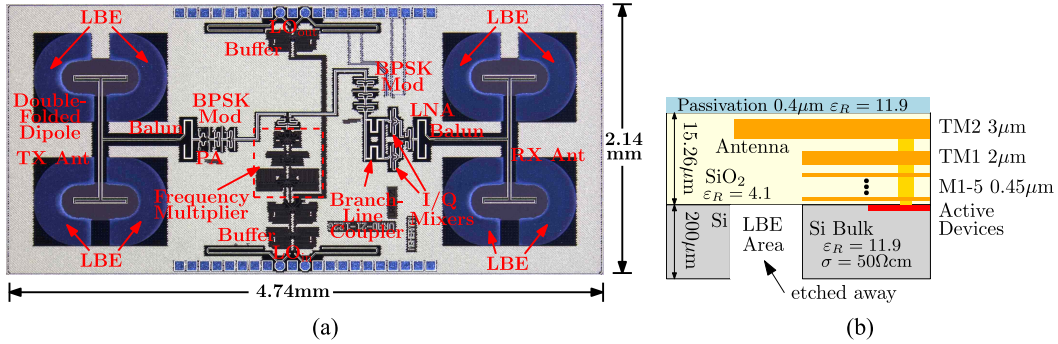


Fig. 7. (a) Chip photograph of the 122-GHz TRX with the on-chip antennas implemented as double-folded dipole antenna using the LBE technique. (b) Cross section of the IHP 130-nm SiGe BiCMOS technology. The antenna is implemented in the TM2 layer.

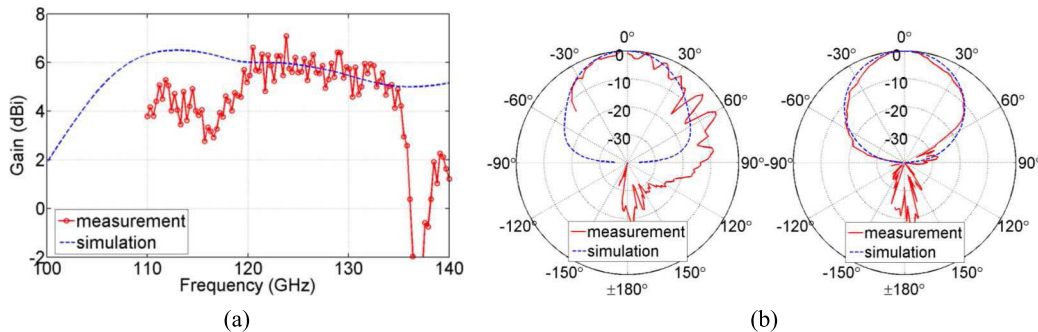


Fig. 8. (a) Measured and simulated gain of the double-folded dipole antenna. (b) Measured and simulated normalized radiation patterns of the double-folded dipole antenna at 122 GHz in *E*-plane (left) and *H*-plane (right).

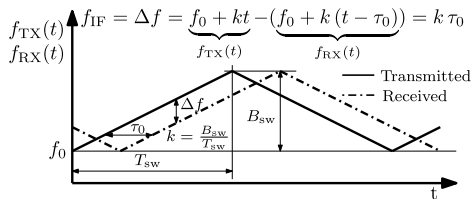


Fig. 9. FMCW frequency course up-chirp and down-chirp. The RTDT τ_0 is directly proportional to the frequency difference of the TX and RX signals.

in [7], [19], [20]. To realize the frequency offsets, those systems rely on external analog building blocks, which are costly and can decrease system performances such as the PN.

Alternatively, a digital offset frequency generation can be realized by using a $\Delta\Sigma$ -modulator in conjunction with a BPSK modulator in the TX path [21]–[24]. Fig. 10 shows the basic principle. Applying the $\Delta\Sigma$ -modulation to a digitally generated sinusoid results in a binary output signal that can be modulated on the TX signal by using the BPSK modulator. The oversampling with the $\Delta\Sigma$ -modulator allows to shape the quantization noise to higher frequencies outside a desired frequency interval. This shaped noise is filtered out in the radar IF signal due to the bandwidth limiting characteristics of several components in the radar systems. The modulation of the carrier signal with the binary-valued $\Delta\Sigma$ -sequence with an equivalent offset frequency f_{OFF} results in a signal component at frequencies $f_{LO} \pm f_{OFF}$ and the $\Delta\Sigma$ noise. The ideal signal model for the resulting IF signal is represented by two complex sinusoids with constant frequencies $f_{OFF} \pm f_{IF}$ and constant

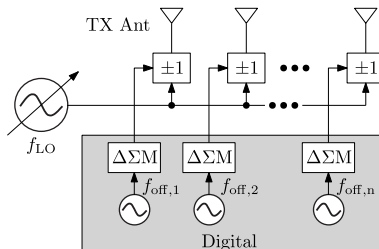


Fig. 10. Block diagram of the $\Delta\Sigma$ modulator-based transmitter.

phase terms $\pm\Phi_0$, as given in

$$S_{IF}(t) = a_{IF}(\exp(j(2\pi(f_{OFF} + f_{IF})t + \Phi_0)) + \exp(j(2\pi(f_{OFF} - f_{IF})t - \Phi_0))) \quad (1)$$

where a_{IF} describes the amplitude of the IF signal, $\Phi_0 = 2\pi f_0 \tau_0 - \pi k \tau_0^2 - \varphi_R$, f_0 is the start frequency, and φ_R is an additional phase shift due to the reflection at the target's surface. The Fourier transformation of the IF signal results in

$$\begin{aligned} S_{IF}(f) &= \int_{-\infty}^{\infty} s_{IF}(t) \cdot \exp(-j2\pi f t) dt \\ &= a_{IF} \cdot \left(\exp(j\Phi_0) \int_{-\infty}^{\infty} \exp(j2\pi(f_{OFF} + f_{IF} - f)t) dt \right. \\ &\quad \left. + \exp(-j\Phi_0) \int_{-\infty}^{\infty} \exp(j2\pi(f_{OFF} - f_{IF} - f)t) dt \right). \end{aligned} \quad (2)$$

For $f = f_{OFF} \pm f_{IF}$, $\exp(j2\pi(f_{OFF} \pm f_{IF} - f)t) = 1 \forall t$, the magnitude of (2) results in a maximum. For

$f \neq f_{\text{OFF}} \pm f_{\text{IF}}$, $\exp(j2\pi(f_{\text{OFF}} \pm f_{\text{IF}} - f)t)$ is a complex sinusoid whose integral over one complete cycle is zero. Therefore, the search for a peak in the magnitude of (2) delivers the frequencies $f_{\text{OFF}} \pm f_{\text{IF}}$. Since f_{OFF} is known, f_{IF} can be easily calculated.

B. Pseudo-Random Noise-Coded Doppler Radar

The multi-purpose radar TRXs can also be used in a distance-selective PRN-coded Doppler radar [10], [25] to measure the vibration/velocity of a target located at a certain distance from the TRX and to suppress all other target responses elsewhere. This is particularly important if the radar measurements have to be done in a noisy environment with many targets and the reflected signal from the particular target at the certain distance is very weak. Fig. 11 shows the basic principle of the proposed architecture using the multi-purpose radar TRX equipped with BPSK modulators. A radar TRX equipped with a down-conversion mixer can extract the Doppler information of any targets located at its beam direction. In order to measure only one target at a certain distance and to suppress all other targets elsewhere, the carrier signal is additionally modulated with a PRBS. The modulated TX signal is radiated in the direction of several targets. A portion of the TX signal is reflected by the targets and received with various time delays that correspond to the distances of the targets from the TRX. The LO signal is also modulated with the same PRBS and mixed with the RX signal to create the IF signal. If the PRBS for the LO signal is delayed by an amount of time corresponding to the distance of the particular target intended to be measured, then the mixing of the LO and the RX signal will produce the IF signal containing the velocity information of the target.

The PRBS $m(t)$ modulated on the TX signal is delayed by the RTDT $\tau(t)$ at the receiver. The same PRBS $m(t)$ is delayed by τ_m and is subsequently modulated on a complex LO signal. The ideal signal model for the resulting IF signal after mixing the LO and RX signal can be written as

$$s_{\text{IF}}(t) = a_{\text{IF}} m \left(t - \underbrace{\left(\tau_0 - \frac{2v_0}{c_0} t \right)}_{\tau(t)} \right) m(t - \tau_m) \\ \cdot \exp \left(j \left(2\pi f_c \underbrace{\frac{2v_0}{c_0} t}_{f_d} - 2\pi f_c \tau_0 + \varphi_R \right) \right) \quad (3)$$

where f_c is the carrier frequency, $\tau_0 = 2r_0/c_0$ is the RTDT at $t = 0$, r_0 is the distance at $t = 0$, and c_0 is the propagation speed of the electromagnetic wave. The term $(2v_0/c_0)t$ is much smaller than the time bin $\Delta\tau = T_{\text{clk}}$ of the PRBS. Due to the Doppler effect, the reflected signal experiences a frequency shift of $f_d = 2f_c v_0/c_0$. For $\tau_m = \tau_0$, $m(t - \tau_0) \cdot m(t - \tau_m) \approx 1 \forall t$, (3) delivers a complex signal with a constant frequency f_d , which can be calculated by using the FFT. For $\tau_m \neq \tau_0$, a sequence, which is spread in the frequency domain, results from $m(t - \tau_0) \cdot m(t - \tau_m)$.

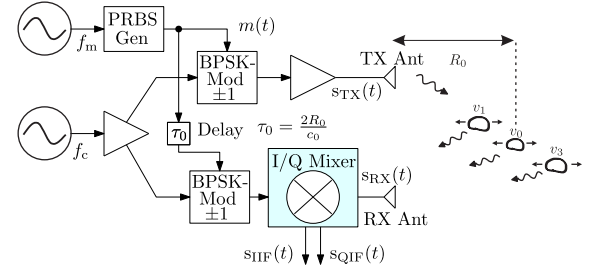


Fig. 11. Basic principle of the distant-selective Doppler radar system using modulated carrier signals. The PRBS for the LO signal is delayed by an amount of time corresponding to the distance of the particular target wished to be measured. The mixing of the LO signal and the RX signal produces the IF signal containing the velocity information of the particular target.

V. RADAR SYSTEM DEMONSTRATOR

The Rogers RO3003 substrate with a thickness of $127 \mu\text{m}$ and a relative dielectric constant of around 3 was chosen for the boards. To stabilize this material, a low-cost FR4 core with a thickness of 1.13 mm was laminated under it.

A. 30.5-GHz PLL

Fig. 12(a) shows the block diagram of the LO signal generation unit consisting of the 30.5-GHz VCO stabilized by the Analog Devices fractional-N PLL chip ADF4159. Fig. 12(b) shows the board and the micrograph of the 30.5-GHz VCO. The chip has a size of $0.94 \times 0.94 \text{ mm}^2$. The differential output signal of the VCO is fed to a balun [26] on the board whose single-ended output is connected to a 1.85-mm SMD connector jack on the board.

The Agilent E5052B signal source analyzer (SSA) was used to measure the PN performance of the VCO and the PLL. The pre-scaler output signal was connected to the SSA and the measurement results were scaled up by adding $20 \log_{10}(16) \text{ dB}$. Fig. 13 shows the measurement results at three different frequencies, which were used as start, center, and stop frequencies for the FMCW radar sweep. The measured PN at 10-kHz offset frequency is -77 dBc/Hz at best and -74 dBc/Hz at worst. The PN is reduced at best to -80 and -106 dBc/Hz at offset frequency of 100 kHz and 1 MHz, respectively.

The frequency ramp generated by the PLL was inspected by using the SSA and the R&S oscilloscope RTO1044. The PLL was configured to generate a triangular waveform with a sweep bandwidth of 2.5 GHz and a sweep length of 1 ms. A delay between each frequency ramp was also programmed to allow for better settling. Fig. 14(a) shows the measured frequency sweep and the resulted voltage ramp at the output of the loop filter. A very small frequency overshoot can be seen at the end of each frequency ramp up and ramp down. As expected, the measured voltage ramp shows a non-linear behavior with a turning point in the middle of the ramp, since the characteristic line of the VCO is also a non-linear function of the tuning voltage. Fig. 14(b) shows the linearity of the frequency sweep. To eliminate the settling behavior of the frequency ramp in the calculation of the frequency error, the first and the last 5% of the sampled data were removed. The frequency error was

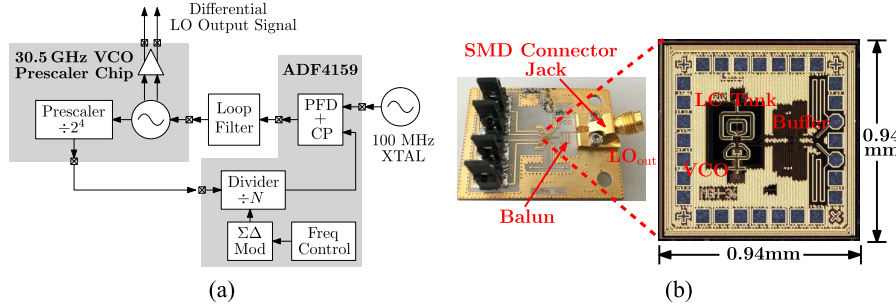


Fig. 12. (a) Simplified block diagram of the LO signal generation unit consisting of the 30.5-GHz VCO stabilized by the analog devices fractional-N PLL chip ADF4159. (b) Board and chip photograph of the 30.5-GHz VCO.

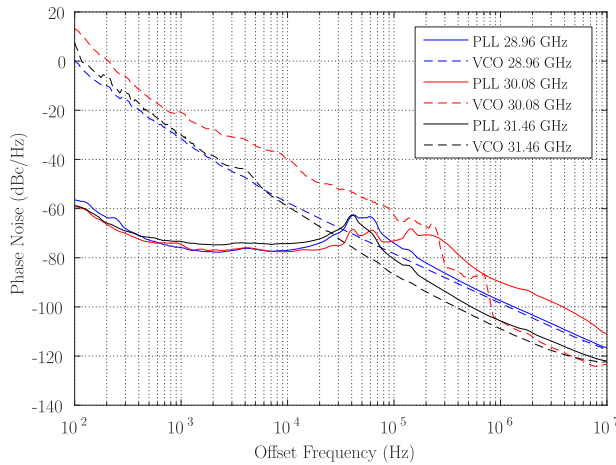


Fig. 13. Measured PN of PLL and VCO.

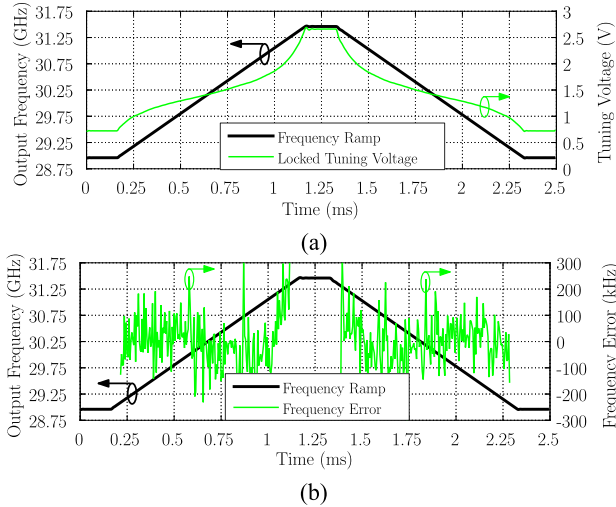


Fig. 14. (a) Measured frequency ramp and tuning voltage of the 30-GHz PLL. (b) Measured frequency error.

determined by calculating the difference between the measured frequencies and a linear fit. The root-mean-square frequency error for the frequency ramp up and ramp down is 418 and 370 kHz, respectively.

B. Radar Frontends

Fig. 15 shows the boards for the 61- and the 122-GHz TRX. The former includes on-board patch array antennas published

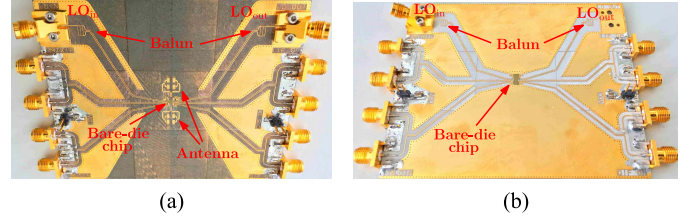


Fig. 15. (a) Board for the 61-GHz TRX with on-board corporate-fed patch array antennas. (b) Board for the 122-GHz TRX with on-chip antennas.

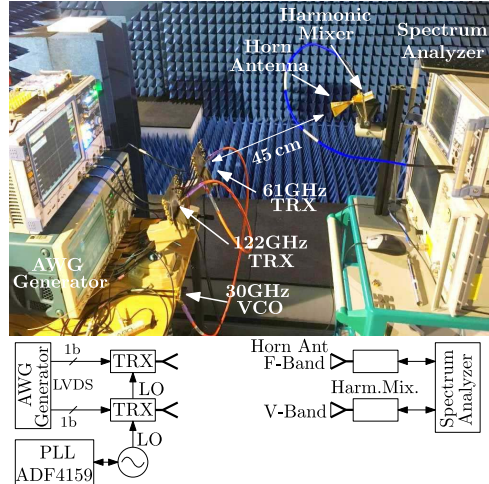


Fig. 16. Photograph of the setup to test the TX functionality of the radar system. A V-band and an F-band horn antennas with a gain of 24 dBi in combination with the corresponding harmonic mixers were connected to the signal analyzer to characterize the modulated TX signals.

in [26]. Each antenna contains four patch elements and four pairs of parasitic elements to have a higher gain and wider bandwidth. This antenna achieves a gain of 9.4–12.4 dBi in a broad frequency range of 57–66 GHz. The boards also include 1.85-mm SMD connector jacks for the LO input and output. These boards are connected to the VCO board by using coaxial cables. Fig. 16 shows the setup to test the TX functionality of the radar system. A V-band horn antenna and an F-band horn antenna with a gain of 24 dBi in combination with the corresponding harmonic mixers were connected to the signal analyzer to characterize the modulated TX signals.

A first-order $\Delta\Sigma$ -modulator was designed in MATLAB and used to generate a bit stream with a length of 1000 for an ideal one-period sinusoid. This bit stream was loaded

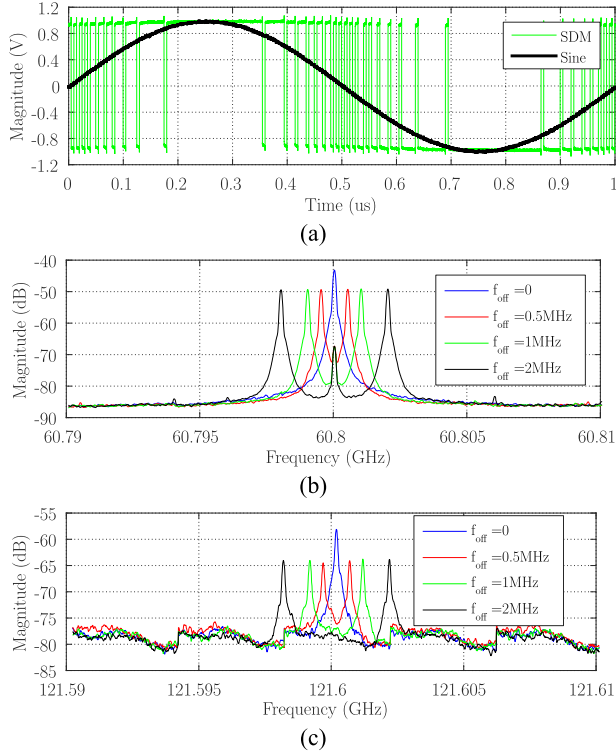


Fig. 17. (a) Input and output waveforms of the first-order $\Delta\Sigma$ -modulator. (b) Spectra of the TX signal of the 61-GHz TRX at different offset frequencies. (c) Spectra of the TX signal of the 122-GHz TRX at different offset frequencies.

into a Tektronix arbitrary waveform generator (AWG) 7102. It was operated with three different clock frequencies of 500 MHz, 1 GHz, and 2 GHz, which in conjunction with the bit stream with the length of 1000 correspond to modulation frequencies of 0.5, 1, and 2 MHz, respectively. Fig. 17(a) shows the waveform of the $\Delta\Sigma$ -modulator. This waveform was modulated on the TX signal by using the BPSK modulator. Fig. 17(b) and (c) shows the spectra of the 61- and the 122-GHz TX signals with different offset frequencies, respectively. As expected, the modulation of the TX signal leads to two signal components at frequencies of $f_{\text{LO}} \pm f_{\text{off}}$.

Almost-perfect autocorrelation sequence (APAS) with a length of 2^{14} was generated in MATLAB and was loaded into the AWG, which was operated with four different clock frequencies from 625 MHz to 5 GHz. Fig. 18(a) shows the waveform of the sequence. This waveform was modulated on the TX signal by using the BPSK modulator. Fig. 18(b) and (c) shows the spectra of the TX signal around the carrier frequencies of 60.8 and 121.6 GHz, respectively. The measured spectra have a form of a sinc function with the first minima corresponding to the clock frequencies of the modulation. Figs. 17 and 18 reveal that the LO leakage in the spectrum of the modulated signal is small. A high LO leakage can reduce the dynamic range of the radar system.

C. Radar Measurement

The applicability of the proposed radar system was demonstrated in the range measurements of static targets in an anechoic chamber. Fig. 19 shows the measurement setup consisting of three corner cubes (CCs) used as static targets,

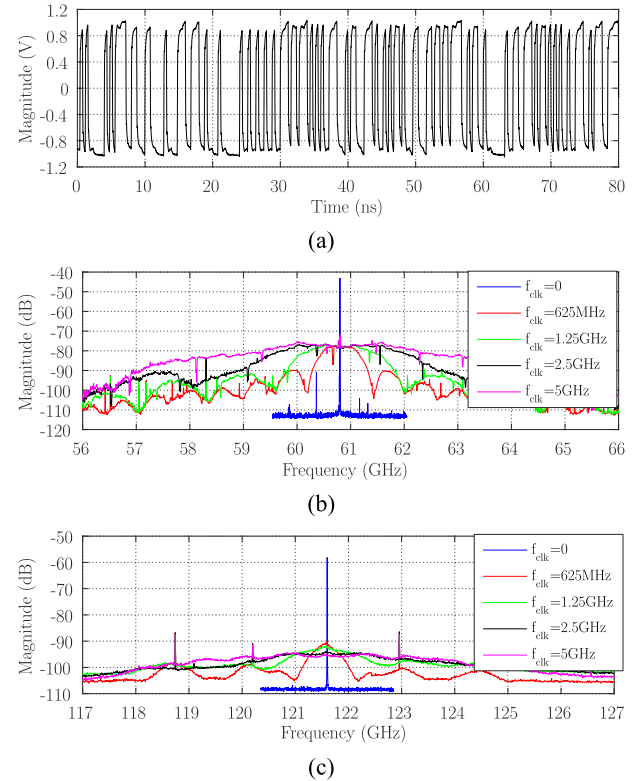


Fig. 18. (a) Waveform of the APAS. (b) Measured spectra of the TX signals around the carrier frequency of 60.8 GHz at different modulation clock frequencies. (c) Measured spectra of the TX signals around the carrier frequency of 121.6 GHz at different modulation clock frequencies.

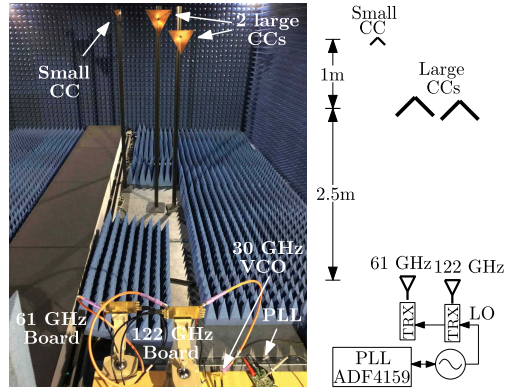


Fig. 19. Radar measurement setup in an anechoic chamber with three CCs as targets. Two CCs with a spacing of 4 cm are located around 2.5 m and one small CC is at 3.5 m from the TRX.

the 61- and the 122-GHz TRXs as well as the 30.5-GHz frequency synthesizer. Two of the CCs have an RCS of 87.7 m^2 at 61 GHz and were placed at a distance of around 2.5 m from the TRXs with a spacing of 4 cm from each other, while one CC has a much smaller RCS of 1.08 m^2 at 61 GHz and was placed at a distance of around 3.5 m from the TRXs. The 30.5-GHz frequency synthesizer was configured to generate a frequency sweep with a bandwidth of 2.5 GHz and a sweep length of 1 ms. This 30.5-GHz LO signal from the frequency synthesizer was fed to the 122-GHz TRX, which output a 30.5-GHz LO signal that was fed to the 61-GHz TRX. The frequency multiplier inside the TRXs multiplies the LO frequency by a factor of 2 or 4. The sweep bandwidth is scaled up to 10 GHz at the 122 GHz and results in a target resolution

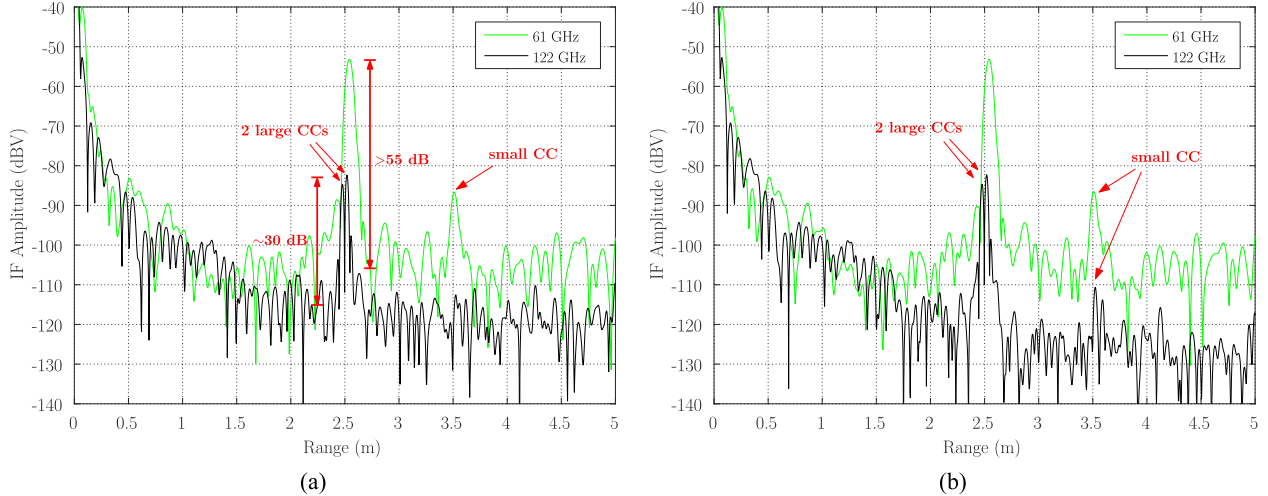


Fig. 20. Measurement results of the three targets (a) without averaging and (b) with averaging over 100 measurements. Note that the two CCs with a spacing of 4 cm can only be resolved with the larger sweep bandwidth of 10 GHz using the 122-GHz TRX, while the small target with a lower reflectivity can only be detected without averaging by the 61-GHz TRX.

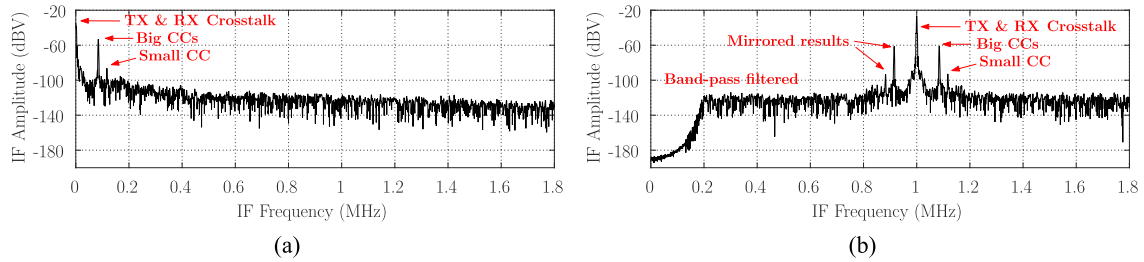


Fig. 21. Results of radar measurement with the 61-GHz TRX. (a) Without $\Delta\Sigma$ -modulation of the TX signal. (b) With $\Delta\Sigma$ -modulation $f_{\text{OFF}} = 1 \text{ MHz}$. Note that the peaks due to the targets are shifted by 1-MHz offset frequency. The two large CCs are shown as one peak and the small CC is visible.

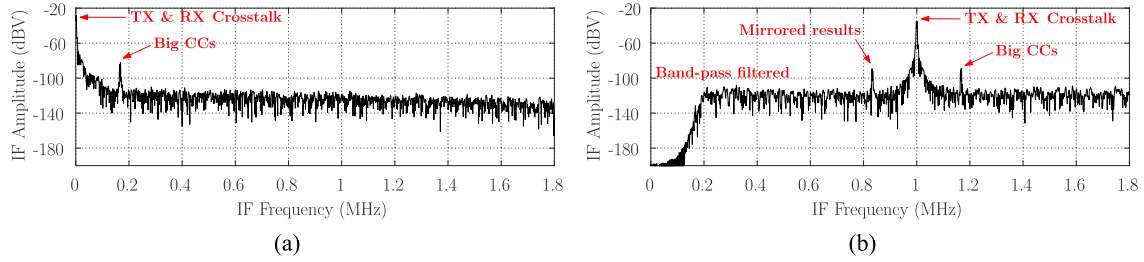


Fig. 22. Results of radar measurement with the 122-GHz TRX. (a) Without $\Delta\Sigma$ -modulation of the TX signal. (b) With $\Delta\Sigma$ -modulation $f_{\text{OFF}} = 1 \text{ MHz}$. Note that the peaks due to the targets are shifted by 1-MHz offset frequency. The two large CCs are shown as two peaks, while the small CC is hidden in the noise floor.

of 100 ps or a range resolution of 1.5 cm if no data windows is used. This range resolution becomes 3 cm if a Hann window is used in the range estimates. At 61-GHz TRX, the configured sweep bandwidth results in a range resolution of 6 cm.

Fig. 20 shows the results of the measurements performed concurrently using the two TRXs without and with averaging. As expected, only the 122-GHz TRX can resolve the two large CCs placed 4 cm from each other, while the measurements with the 61-GHz TRX resulted in only one peak for the targets. Note that the SNR of the peaks measured using the 61-GHz TRX is around 25 dB better compared with the result of the 122-GHz TRX due to the higher TX output power, higher antenna gain, and lower noise figure of the 61-GHz TRX. Without averaging, the small CC with the RCS of 1.08 m^2 at 61 GHz can only be detected by the 61-GHz TRX, which has a higher dynamic range. It is hidden in the noise floor

in the result measured by the 122-GHz TRX. With averaging from 100 measurements, the noise floor is reduced so that the small CC is shown as a peak in the IF spectrum of the 122-GHz TRX.

The $\Delta\Sigma$ -modulation was applied in the FMCW radar. A bit sequence with a length of 1000 for an ideal one-period sinusoid was generated in MATLAB and loaded into the Tektronix AWG 7102, which was operated with a sample rate of 1 GHz. This configuration results in a corresponding offset frequency of 1 MHz. This bit stream was then modulated on the BPSK modulator of the TX path. The same measurement setup consisting of two large CCs and one small CC and the same frequency ramp setup with 2.5-GHz sweep bandwidth and a sweep period of 1 ms were used for these measurements. The measurement results using the 61- and 122-GHz TRX are shown in Figs. 21 and 22, respectively. The measurement

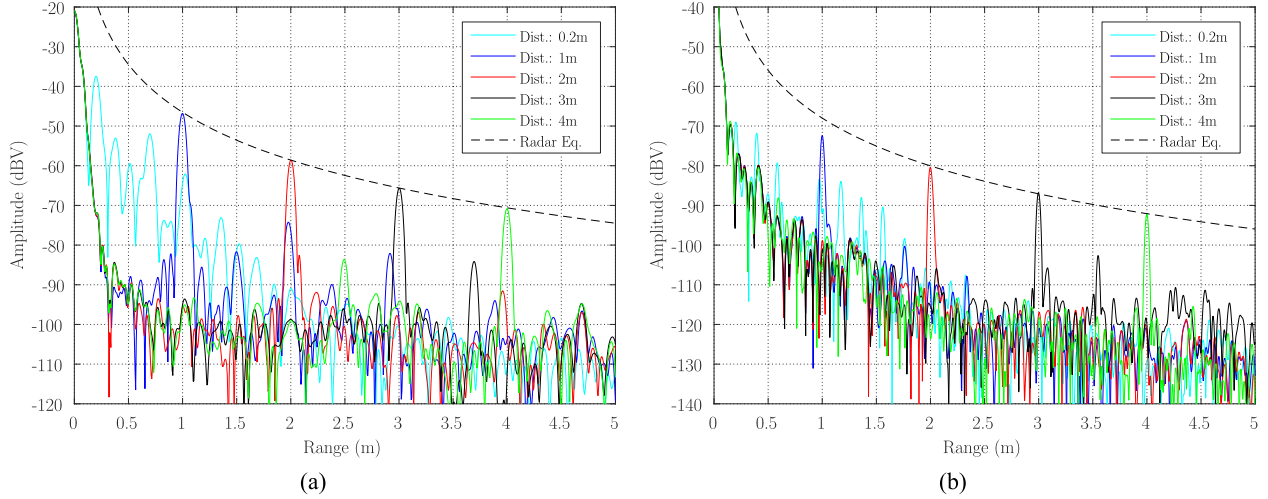


Fig. 23. Radar measurement results with a single target located at different positions using (a) 61-GHz TRX with a sweep bandwidth of 5 GHz and (b) 122-GHz TRX with a sweep bandwidth of 10 GHz. Note that the IF amplitudes at higher ranges follow the radar equation. The peaks of the measurements using the 122-GHz TRX are narrower due to the higher resolution. The radar system is able to detect target as close as 0.2 m.

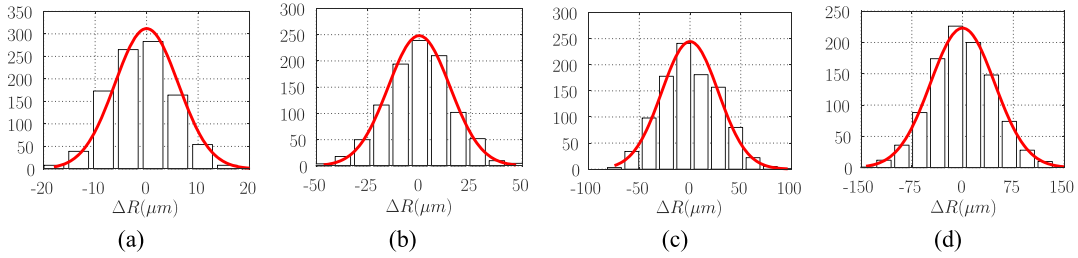


Fig. 24. Histogram of the deviations of the 1000 range estimates subtracted from the mean of the measurements using the 61-GHz TRX at (a) $R = 1$ m, (b) $R = 2$ m, (c) $R = 3$ m, and (d) $R = 4$ m. Note that the Gaussian bell curves become broader and the peaks become lower with increasing ranges due to decreasing SNR.

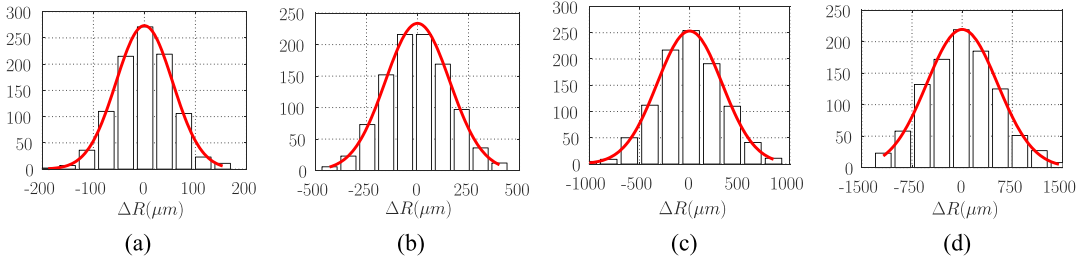


Fig. 25. Histogram of the deviations of the 1000 range estimates subtracted from the mean of the measurements using the 122-GHz TRX at (a) $R = 1$ m, (b) $R = 2$ m, (c) $R = 3$ m, and (d) $R = 4$ m. Note that the Gaussian bell curves are at least ten times broader compared with the results of the 61-GHz TRX.

results using the delta-sigma modulated signals were filtered using a fifth-order Chebyshev bandpass filter to filter out the $\Delta \Sigma$ noise at higher frequency and to remove the dc part of the signal, which is irrelevant for the range estimates. As expected, applying the delta-sigma modulation on the TX signal results in a frequency shift in the IF spectrum. The distinction of the TX channels can be achieved by applying different delta-sigma modulations corresponding to different frequency shifts. Note that the results of the frequency estimates are similar to previous results. The two peaks with a spacing of 4 cm can only be resolved as two targets in the measurement results using the 122-GHz TRX due to a higher modulation

bandwidth, while the small CC can only be seen in the measurement results using the 61-GHz TRX due to a higher dynamic range.

Radar measurements of a single target located at different positions between 0.2 and 4 m were performed to inspect the accuracy of the radar systems. The same frequency ramp setup (2.5-GHz frequency sweep at 30.5-GHz LO frequency and 1-ms sweep length) was used for these measurements. The 1000 measurements were performed for each different position of the target. The resulting plots of the measured IF signals are shown in Fig. 23, which shows the peaks at the correct positions of the target. At positions close to the

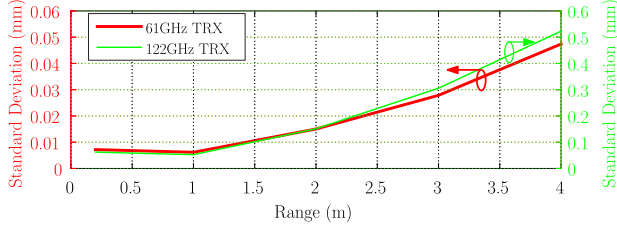


Fig. 26. Standard deviations of the 1000 range measurements using the 61- and the 122-GHz radar TRXs at varying target positions. Note that due to the higher dynamic range, the ranging accuracy of the 61-GHz radar TRX is around ten times higher than the 122-GHz radar TRX. The standard deviations of the range estimates increase with increasing target distances due to the decreasing SNR.

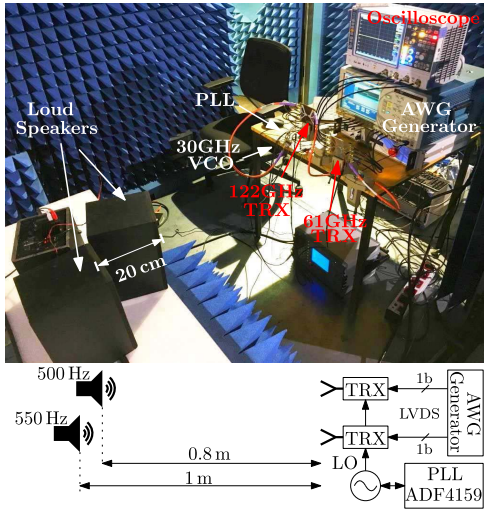


Fig. 27. Setup for the distance-selective vibration measurements in an anechoic chamber using the 61- and the 122-GHz PRN-coded Doppler radars. Two loudspeakers were used as targets, the first vibrated with a frequency of 500 Hz and was located at 0.8 m, while the second vibrated with a frequency of 550 Hz and was located at 1 m from the TRXs.

TRXs, the multi-path reflections between the demonstrator board and the target result in additional peaks at different ranges corresponding to the paths traveled by the waves. The measured amplitudes of the IF signals closely follow the radar equation. The histograms of the range measurements using the 61- and 122-GHz TRX for four different positions are shown in Figs. 24 and 25, respectively. The results show a symmetric normal distribution without any visible outliers. The Gaussian bell curves become broader with increasing ranges. The standard deviation (σ) for varying distances is shown in Fig. 26. As expected, the σ value increases with increasing target distances due to the decreasing SNR. The σ value of the 61-GHz TRX is at least ten times lower compared with the σ value of the 122-GHz TRX, which has a lower dynamic range.

The capability of the TRXs in the detection of a vibration/velocity at a specified distance was demonstrated in measurements in an anechoic chamber. Fig. 27 shows the measurement setup consisting of two loudspeakers used as targets, the 61- and 122-GHz TRXs, and the AWG used to generate the PRBSs. MATLAB was used to create a wave file

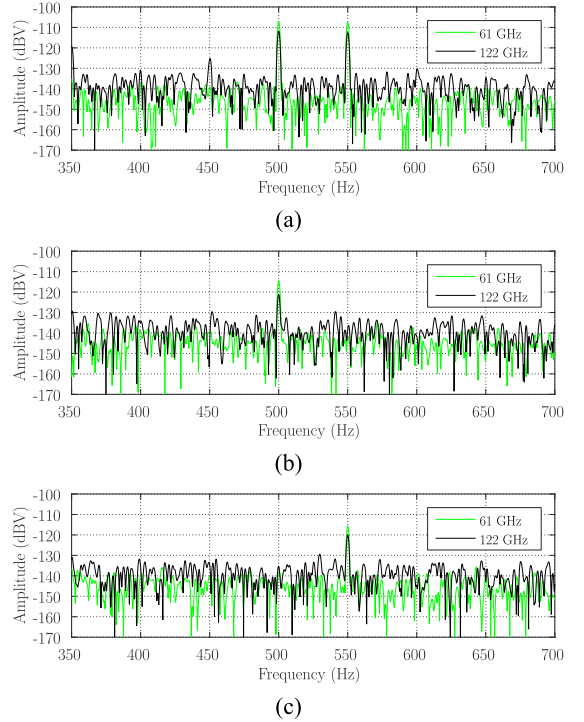


Fig. 28. Vibration measurement of loudspeakers with the 61-GHz and 122-GHz TRXs. (a) Result of the conventional Doppler mode with deactivated PRN modulation, and it shows the vibrations of both loudspeakers. (b) Result of the PRN mode with a delay setup corresponding to a range 0.8 m, and it shows the vibration of the first loudspeaker, while the vibration of the second loudspeaker is suppressed. (c) Result of the PRN mode with a delay setup corresponding to a range of 1 m, and it shows the vibration of the second loudspeaker, while the vibration of the first loudspeaker is suppressed. The SNR in the measurement results of the 61-GHz TRX is higher than the SNR of the 122-GHz TRX.

containing two sine wave tones with the frequencies of 500 and 550 Hz. This stereo file was played on a computer of which audio output was connected to the two loudspeakers. The first loudspeaker vibrated with 500 Hz and was placed at 0.8 m, while the second vibrated with 550 Hz and was located at 1 m from the TRXs. The AWG generated two APASs with a length of 2^{14} . The first sequence is modulated on the TX signal, while the second sequence, which is a delayed version of the first, was modulated on the LO signal used to down-convert the RX signal. This delay should correspond to the range of the targets to be detected. The sequences were generated with a clock frequency of 5 GHz, which corresponds to a range resolution of 3 cm. The second sequence had to be delayed by 26 and 33 clock periods to detect the loudspeakers at 0.8 and 1 m, respectively. The IF signals were converted to the digital domain by using the R&S oscilloscope RTO1044 and FFT was performed on the results. Fig. 28 shows the measurement results. If the modulation is disabled, the TRXs act as simple Doppler radar TRXs and deliver the Doppler frequency shifts of 500 and 550 Hz caused by the vibration of the two loudspeakers. From these results, one has no information about which loudspeaker results in lower and which loudspeaker results in the higher Doppler frequency. If the carrier signals are additionally modulated with the PRN sequences, then the TRXs have the ability to select which

TABLE II
COMPARISON OF STATE-OF-THE-ART 61- AND 122-GHz SiGe TRXs

Ref	[27]	[28]	[29]	This work	[30]	[31]	[32]	This work
Freq(GHz)	60	60	60	61	122	122	125	122
PN(dBc/Hz) ¹	-105 ²	-80	-89	-100	-92 ²	-100 ²	-	-94
P _{TX} (dBm)	4	10.7	13.4 to 16.2	11.5	-2.5	3.6	3.2	5
G _{RX} (dB)	19	32	70 to 72	24	25	13	15.5 ³	21
P _{1dB} (dBm)	-8.5	-30	-70	-12	-25	-20	-	-11
Noise Fig.(dB)	9.5	7	7	9.8 ⁴	-	11.5	9.5 ^{3,4}	12.7 ⁴
P _{DC} (mW)	990 ⁵	924	1060	594	380	900	-	627
Mod.BW(GHz)	7	2	-	5	3.7	8.7	30	10
Range Res.(cm)	4.28	15	-	6	8.1	3.4	1.05	3
Range σ(μm) ⁶	-	80	-	6.1	-	-	-	52.5
Ant. Architecture	eWLB package single patch	eWLB package single patch	Integrated package	Board patch array	On-chip patch+quartz resonator	On-chip single dipole	On-chip double-folded dipole+LBE	
Ant. Gain (dBi)	6	8	8	9.4 to 12.4	-	6	1.8 to 4 ⁶	6

¹at 1-MHz offset frequency, ²VCO only, ³LNA only without mixer, ⁴simulation result only, ⁵4RX+2TX, ⁶at 1-m distance.

target to be measured and which target to be ignored or suppressed. In Fig. 28(b), the second sequence used to modulate the LO signal is delayed by a value corresponding to a range of 0.8 m. So only the first loudspeaker can be detected, while the vibration of the second loudspeaker is suppressed. The results show the Doppler frequency shift of 500 Hz. In Fig. 28(c), the delay of the second sequence corresponds to a range of 1 m. The results clearly show the Doppler frequency shift of 550 Hz, which is the vibration frequency of the second loudspeaker. The SNR in the measurement results of the 61-GHz TRX is higher compared with the SNR of the 122-GHz TRX.

VI. CONCLUSION

A scalable radar system that provides optimal dynamic range, resolution, and miniaturization degree by utilizing multi-band TRXs is presented. The proposed architecture enables the cascading of multiple TRXs by using a single 30.5-GHz LO signal that can be routed easily to each of the TRX without any additional LO distribution network. The TRXs are equipped with a frequency multiplier, an I/Q receiver as well as BPSK modulators and allow to build flexible MIMO radar sensor applications utilizing PRN and FMCW radar techniques with the ΔΣ-modulator-based FDM. A summary of recent publications of 61- and 122-GHz (radar) TRXs in SiGe technologies is shown in Table II. The 61-GHz TRX achieves a σ of 6.1 μm at 1-m distance, while a range resolution of 3 cm can be achieved by using the 122-GHz TRX, which is equipped with an integrated on-chip antenna with a gain of 6 dBi. Both TRXs can also be used for distant-selective vibration measurements. Various radar measurements confirm the applicability and the flexibility of the proposed scalable sensor system that can be used for the software-defined radar platform.

REFERENCES

- H. Rucker *et al.*, “A 0.13 μm SiGe BiCMOS technology featuring f_T/f_{max} of 240/330 GHz and gate delays below 3 ps,” *IEEE J. Solid-State Circuits*, vol. 45, no. 9, pp. 1678–1686, Oct. 2010.
- M. Schroeter *et al.*, “SiGe HBT technology: Future trends and TCAD-based roadmap,” *Proc. IEEE*, vol. 105, no. 6, pp. 1068–1086, Jun. 2017.
- S. P. Voinigescu, S. Shopov, J. Hoffman, and K. Vasilakopoulos, “Analog and mixed-signal millimeter-wave SiGe BiCMOS circuits: State of the art and future scaling,” in *Proc. IEEE Compound Semicond. Integr. Circuit Symp. (CSICS)*, Oct. 2016, pp. 1–4.
- H. J. Ng, M. Kucharski, and D. Kissinger, “Scalable sensor platform with multi-purpose fully-differential 61 and 122 GHz transceivers for MIMO radar applications,” in *Proc. IEEE Bipolar/BiCMOS Circuits Technol. Meeting (BCTM)*, Sep. 2016, pp. 170–173.
- H. J. Ng, J. Wessel, D. Genschow, R. Wang, Y. Sun, and D. Kissinger, “Miniatirized 122 GHz system-on-chip radar sensor with on-chip antennas utilizing a novel antenna design approach,” in *IEEE MTT-S Int. Microw. Symp. Dig.*, May 2016, pp. 1–4.
- T. Spreng, S. Yuan, V. Valenta, H. Schumacher, U. Siart, and V. Ziegler, “Wideband 120 GHz to 140 GHz MIMO radar: System design and imaging results,” in *Proc. Eur. Microw. Conf. (EuMC)*, Sep. 2015, pp. 430–433.
- C. Pfeffer, R. Feger, C. Wagner, and A. Stelzer, “FMCW MIMO radar system for frequency-division multiple TX-beamforming,” *IEEE Trans. Microw. Theory Techn.*, vol. 61, no. 12, pp. 4262–4274, Dec. 2013.
- H. J. Ng, R. Feger, and A. Stelzer, “A fully-integrated 77-GHz UWB pseudo-random noise radar transceiver with a programmable sequence generator in SiGe technology,” *IEEE Trans. Circuits Syst. I, Reg. Papers*, vol. 61, no. 8, pp. 2444–2455, Aug. 2014.
- H. J. Ng, R. Feger, C. Wagner, and A. Stelzer, “A fully-integrated 77-GHz radar transceiver using two programmable pseudo-random sequences,” in *Proc. 11th Eur. Radar Conf.*, Oct. 2014, pp. 293–296.
- H. J. Ng, R. Feger, and A. Stelzer, “A fully-integrated 77-GHz pseudo-random noise coded doppler radar sensor with programmable sequence generators in SiGe technology,” in *IEEE MTT-S Int. Microw. Symp. Dig.*, Jun. 2014, pp. 1–4.
- M. G. M. Notten and H. Veenstra, “60 GHz quadrature signal generation with a single phase VCO and polyphase filter in a 0.25 μm SiGe BiCMOS technology,” in *Proc. IEEE Bipolar/BiCMOS Circuits Technol. Meeting*, Monterey, CA, USA, Oct. 2008, pp. 178–181.
- H. Li and H. M. Rein, “Millimeter-wave VCOs with wide tuning range and low phase noise, fully integrated in a SiGe bipolar production technology,” *IEEE J. Solid-State Circuits*, vol. 38, no. 2, pp. 184–191, Feb. 2003.
- H. Li, H. M. Rein, T. Suttorp, and J. Bock, “Fully integrated SiGe VCOs with powerful output buffer for 77-GHz automotive radar systems and applications around 100 GHz,” *IEEE J. Solid-State Circuits*, vol. 39, no. 10, pp. 1650–1658, Oct. 2004.
- Y. Sun and C. Scheytt, “A low-phase-noise 61 GHz push-push VCO with divider chain and buffer in SiGe BiCMOS for 122 GHz ISM applications,” in *Proc. IEEE Radio Freq. Integr. Circuits Symp. (RFIC)*, Jun. 2012, pp. 79–82.
- R. Wang, Y. Sun, M. Kaynak, S. Beer, J. Borngräber, and J. C. Scheytt, “A micromachined double-dipole antenna for 122–140 GHz applications based on a SiGe BiCMOS technology,” in *IEEE MTT-S Int. Microw. Symp. Dig.*, Jun. 2012, pp. 1–3.

- [16] M. I. Skolnik, *Radar Handbook*, 2nd ed. Boston, MA, USA: McGraw Hill, 1988.
- [17] B. Huder, *Einführung in die Radartechnik*. Stuttgart, Germany: B. G. Teubner, 1999.
- [18] A. G. Stove, "Linear FMCW radar techniques," *IEE Proc. F-Radar Signal Process.*, vol. 139, no. 5, pp. 343–350, Oct. 1992.
- [19] R. Feger, C. Wagner, and A. Stelzer, "An IQ-modulator based heterodyne 77-GHz FMCW radar," in *Proc. German Microw. Conf.*, Mar. 2011, pp. 1–4.
- [20] C. Pfeffer, R. Feger, C. M. Schmid, C. Wagner, and A. Stelzer, "An IQ-modulator based heterodyne 77-GHz FMCW colocated MIMO radar system," in *IEEE MTT-S Int. Microw. Symp. Dig.*, Jun. 2012, pp. 1–3.
- [21] R. Feger, H. J. Ng, C. Pfeffer, and A. Stelzer, "A delta-sigma transmitter based heterodyne FMCW radar," in *Proc. Eur. Radar Conf.*, Oct. 2013, pp. 208–211.
- [22] R. Feger, H. J. Ng, C. Pfeffer, and A. Stelzer, "A delta-sigma modulator-based heterodyne FMCW radar for short-range applications," *Int. J. Microw. Wireless Technol.*, vol. 6, nos. 3–4, pp. 379–387, Jun. 2014.
- [23] R. Feger, C. Pfeffer, and A. Stelzer, "A frequency-division MIMO FMCW radar system using delta-sigma-based transmitters," in *IEEE MTT-S Int. Microw. Symp. Dig.*, Jun. 2014, pp. 1–4.
- [24] R. Feger, C. Pfeffer, and A. Stelzer, "A frequency-division MIMO FMCW radar system based on delta-sigma modulated transmitters," *IEEE Trans. Microw. Theory Techn.*, vol. 62, no. 12, pp. 3572–3581, Dec. 2014.
- [25] P. Heide, V. Magori, and R. Schwarte, "Coded 24 GHz doppler radar sensors: A new approach to high-precision vehicle position and ground-speed sensing in railway and automobile applications," in *IEEE MTT-S Int. Microw. Symp. Dig.*, vol. 2. Orlando, FL, USA, May 1995, pp. 965–968.
- [26] R. Wang, Y. Sun, C. Wipf, and J. C. Scheytt, "An on-board differential patch array antenna and interconnects design for 60 GHz applications," in *Proc. IEEE Int. Conf. Microw., Commun., Antennas Electron. Syst. (COMCAS)*, Nov. 2011, pp. 1–5.
- [27] I. Nasr *et al.*, "A highly integrated 60 GHz 6-channel transceiver with antenna in package for smart sensing and short-range communications," *IEEE J. Solid-State Circuits*, vol. 51, no. 9, pp. 2066–2076, Sep. 2016.
- [28] C. Beck *et al.*, "Industrial mmWave radar sensor in embedded wafer-level BGA packaging technology," *IEEE Sensors J.*, vol. 16, no. 17, pp. 6566–6578, Sep. 2016.
- [29] A. Tomkins *et al.*, "A 60 GHz, 802.11ad/WiGig-compliant transceiver for infrastructure and mobile applications in 130 nm SiGe BiCMOS," *IEEE J. Solid-State Circuits*, vol. 50, no. 10, pp. 2239–2255, Oct. 2015.
- [30] W. Debski, W. Winkler, Y. Sun, M. Marinkovic, J. Borngraber, and J. C. Scheytt, "120 GHz radar mixed-signal transceiver," in *Proc. 7th Eur. Microw. Integr. Circuits Conf. (EuMIC)*, Oct. 2012, pp. 191–194.
- [31] I. Sarkas, J. Hasch, A. Balteanu, and S. P. Voinigescu, "A fundamental frequency 120-GHz SiGe BiCMOS distance sensor with integrated antenna," *IEEE Trans. Microw. Theory Techn.*, vol. 60, no. 3, pp. 795–812, Mar. 2012.
- [32] S. Yuan and H. Schumacher, "110–140-GHz single-chip reconfigurable radar frontend with on-chip antenna," in *Proc. IEEE Bipolar/BiCMOS Circuits Technol. Meeting (BCTM)*, Oct. 2015, pp. 48–51.



Herman Jalli Ng (M'16) was born in Indonesia in 1981. He received the Dipl.-Ing. degree (Hons.) in communication engineering from the University of Applied Sciences, Karlsruhe, Germany, in 2005, and the Dr.techn. (Ph.D.) degree in mechatronics from Johannes Kepler University, Linz, Austria, in 2014.

From 2005 to 2009, he was with Robert Bosch GmbH, Reutlingen, Germany, as an IC Design Engineer, where he was involved in developing mixed-signal ASICs in HV-CMOS and BCD technologies for automotive sensors. In 2009, he joined the Institute for Communications and Information Engineering, Johannes Kepler University, as a Research Assistant, where he became a member of the Christian Doppler Laboratory for Integrated Radar Sensors in 2011. In 2015, he joined IHP GmbH, Frankfurt (Oder), Germany, where he currently heads the Millimeter-Wave Wireless Group. His current research interests include integrated radar sensors, frequency synthesizers, and analog/RF and mixed-signal circuits.



Maciej Kucharski (M'16) received the B.Sc. degree in electrical engineering from the Warsaw University of Technology, Warsaw, Poland, in 2012, and the M.Sc. degree in computer engineering from the Technical University of Berlin, Berlin, Germany, in 2015. He is currently pursuing the Ph.D. degree with IHP GmbH, Frankfurt (Oder), Germany.

Since 2014, he has been with the IHP GmbH. His current research interests include integrated RF front-ends, radar sensors, and frequency synthesizers.



Wael Ahmad received the BSEE and MSEE degrees from Ain Shams University, Cairo, Egypt, in 2007 and 2012, respectively.

He has been holding engineering positions with RF Industries, Inc., Cairo, Egypt, since 2008, including RF/Microwave Hardware Design and PA Product Development in Egypt. Since 2016, he has been involved in mm-Wave wireless radar components and systems with IHP GmbH, Frankfurt (Oder), Germany, as a Circuit Design Scientist.



Dietmar Kissinger (S'08–M'11–SM'14) received the Dipl.-Ing., Dr.-Ing., and Habilitation degrees in electrical engineering from Friedrich-Alexander-Universität Erlangen-Nürnberg, Erlangen, Germany, in 2007, 2011, and 2014, respectively.

From 2007 to 2010, he was with Danube Integrated Circuit Engineering, Linz, Austria, where he was a System and Application Engineer with the Automotive Radar Group. From 2010 to 2014, he was a Lecturer and the Head of the Radio Frequency Integrated Sensors Group, Institute for Electronics Engineering, Erlangen. Since 2015, he has been a Full Professor with the Technische Universität Berlin, Berlin, Germany, and the Head of the Circuit Design Department, IHP GmbH, Frankfurt (Oder), Germany. He is currently a Co-Director of the Joint Lab for Radio Frequency Integrated Systems, Friedrich-Alexander-Universität Erlangen-Nürnberg. He has authored or co-authored over 200 technical papers and holds several patents. His current research interests include silicon high-frequency and high-speed and low-power integrated systems for communication and automotive, industrial, security, and biomedical sensing applications.

Dr. Kissinger was a member of the 2013 and 2017 European Microwave Week Organizing Committee. He is a member of the European Microwave Association, the German Information Technology Society, and the Society of Microelectronics, Microsystems and Precision Engineering. He serves as a member of Biological Effects and Medical Applications (MTT-10). He is an Elected Member of the IEEE MTT-S Administrative Committee. He is an Executive Committee Member of the IEEE Topical Meeting on Silicon Monolithic Integrated Circuits in RF Systems and a Steering Committee Member of the IEEE Radio Wireless Symposium. He received the 2017 IEEE MTT-S Outstanding Young Engineer Award and was a co-recipient of several best paper awards. He also serves as the Chair of the IEEE MTT-S Technical Committee Microwave and Millimeter-Wave Integrated Circuits (MTT-6). He was the two-time Chair of the IEEE Topical Conference on Wireless Sensors and Sensor Networks and the two-time Chair of the IEEE Topical Conference on Biomedical Wireless Technologies, Networks and Sensing Systems. He was a five-time Guest Editor of the *IEEE Microwave Magazine* and served as an Associate Editor of the *IEEE TRANSACTIONS ON MICROWAVE THEORY AND TECHNIQUES*.